Assessing the influence of van der Waals corrected exchange-correlation functionals on the anisotropic mechanical properties of coinage metals

Ji-Hwan Lee, Jong-Hun Park, and Aloysius Soon*

Global E^3 Institute and Department of Materials Science and Engineering, Yonsei University, Seoul 120-749, Korea

(Received 12 April 2016; revised manuscript received 17 June 2016; published 11 July 2016)

Current materials-related calculations employ density-functional theory (DFT), commonly using the (semi-) local-density approximations for the exchange-correlation (xc) functional. The difficulties in arriving at a reasonable description of van der Waals (vdW) interactions by DFT-based models is to date a big challenge. In this work, we use various flavors of vdW-corrected DFT xc functionals—ranging from the quasiempirical force-field add-on vdW corrections to self-consistent nonlocal correlation functionals—to study the bulk lattice and mechanical properties (including the elastic constants and anisotropic indices) of the coinage metals (copper, silver, and gold). We critically assess the reliability of the different vdW-corrected DFT methods in describing their anisotropic mechanical properties which have been less reported in the literature. In the context of this work, we regard that our results reiterate the fact that advocating a so-called perfect vdW-inclusive xc functional for describing the general physics and chemistry of these coinage metals could be a little premature. These challenges to modern-day functionals for anisotropically strained coinage metals (e.g., at the faceted surfaces of nanostructures) may well be relevant to other strained material systems.

DOI: 10.1103/PhysRevB.94.024108

I. INTRODUCTION

It is undisputed that density-functional theory (DFT) calculations have been commonly used for computational studies of modern-day materials [1]. Despite its popularity and recognition, the commonly used (semi)local approximations to the exchange-correlation (xc) functionals are still, to date, plagued by their failure to account for and describe the critical role of long-range van der Waals (vdW)–type interactions for many molecular and solid-state systems [2–4].

Of late, there have been various attempts to incorporate vdW-type corrections in standard DFT calculations. This has been nicely reviewed in recent literature, e.g., in Refs. [2,5,6]. Broadly speaking, these vdW correction schemes may be classified into two main categories: (1) the dispersion energy (E_{disp}) add-on corrections to standard xc functionals and (2) self-consistent nonlocal correlation functionals.

In the dispersion energy correction scheme, the dispersion energy (E_{disp}) is often added onto the DFT energy (E_{DFT}) where the total energy, $E_{\text{tot}} = E_{\text{DFT}} + E_{\text{disp}}$. This dispersive interaction term is routinely computed via the dispersion coefficient, C_x. Here, C_x is xth-order coefficient of the attractive $1/r^x$ asymptotic potential. Examples of this scheme are the empirical force-field correction approach due to Grimme *et al.* [4,7,8] and the Tkatchenko-Scheffler (TS) approach [9,10] where the dispersion coefficients and damping function are determined self-consistently from the electron charge density.

The former Grimme's vdW correction approach is geometry dependent and largely relies on the local coordination of each atom to scale the atomic C_6 coefficient in a pairwise fashion [8]. In this case, either the zero damping method (D3) or the damping method due to Becke and Johnson (D3BJ) is usually adopted in the Grimme scheme. It was proposed that the D3BJ correction may provide a better description of anisotropies in materials over the D3 method [2,8].

On the other hand, the TS scheme and its variants calculate the effective atomic polarizability and the C_6 values via the Hirshfeld partitioning method to account for the local chemical environment [9]. In hope to improve the TS method for solid-state systems, a self-consistent screening (TS+SCS) recipe was suggested to obtain more accurate values of the C_6 coefficient [10]. For bulk ionic solids, a further improved iterative Hirshfeld partitioning scheme (TS+HI) has been proposed to address the failure of the conventional Hirshfeld partitioning method to adequately describe the structure and energetics of these ionic solids [11].

Turning now to the self-consistent nonlocal correlation functionals, the common practice here is to treat the nonlocal correlation energy term, E_c^{nl}, via an explicit inclusion of the nonlocal (e.g., long-range London dispersion interactions) to the (semi)local correlation functionals in a self-consistent way [12–17]. These so-called vdW density functionals (vdW-xc) reformulate the xc energy, E_{xc}, by keeping the generalized gradient approximation (GGA) exchange energy, $E_{\text{x}}^{\text{GGA}}$, while replacing the GGA correlation energy with a certain proportion of the local-density approximation (LDA) correlation energy, $E_{\text{c}}^{\text{LDA}}$, and the E_c^{nl} [15], where $E_{\text{xc}} = E_{\text{x}}^{\text{GGA}} + aE_{\text{c}}^{\text{LDA}} + bE_c^{\text{nl}}$. This results in various flavors of vdW-corrected xc functionals with different underlying GGAs such as vdW-DF1, vdW-DF2, optPBE, optB88, and opt86B, just to name a few [2,15–18].

To date, much work and progress in applying these vdW corrections have been focused on affording a more accurate description of weak interlayer bonding properties of low-dimensional materials, in particular to various conjugated π-π molecular systems and the recently discovered two-dimensional (2D) nanomaterials (e.g., graphene and transition-metal dichalcogenides) where weak vdW effects may be dominant [19–26]. It was noted that the influence of vdW forces on the fundamental bonding properties, such as lattice constants, cohesion, and sliding mechanisms, are

*Corresponding author: aloysius.soon@yonsei.ac.kr

non-negligible, and its repercussion on the mechanical properties of these nanomaterials is still an open question [23,24,26,27].

On this note, the understanding of the influence of vdW in more complex bulk systems, e.g., transition metals, is far from complete. It was first reported in the seminal work of Rehr, Zaremba, and Kohn, where they estimated that the nontrivial contribution of vdW effects to the cohesive energy (on a per atom basis) is about 6%, 14%, and 16% for Cu, Ag, and Au, respectively [28]. The impact on this non-negligible vdW contribution to their metal bonds may have far-reaching implications—from surface chemical catalysis to mechanoelectronic surface responses, e.g., in molecule-metal bond formation via surface adsorption processes and work function modulations of these coinage metals under stress and/or strain [29,30]. It is only recently that we have begun to appreciate and develop an interest in a more accurate description of vdW effects in these bulk metals and their surfaces [31,32].

Given that metals are well thought of as a delicate interplay between delocalized nearly free electrons and polarizable ionic cores, it is not clear if current approximate theories and implementation of vdW corrections may adequately describe this interplay satisfactorily. It is indeed questionable if the commonly ascribed force-field Grimme's dispersion correction scheme (which is based on a pairwise-additive, localized atom-based description of dispersion forces) is really appropriate for metals.

In this sense, it is aim of this work to examine and assess the influence of the vdW corrections to semilocal functionals on the equilibrium properties of the coinage metals (Cu, Ag, and Au), as well as to use these metals as a test case to investigate the impact of vdW corrections to describe their stretch metal bonds under anisotropic mechanical stress and/or strain. In particular, using current vdW-corrected xc DFT functionals, we calculate their angular-dependent (anisotropic) Young's modulus and Poisson's ratio, as well as well-defined elastic anisotropic indices to compare with available experimental values.

II. METHODOLOGY AND COMPUTATIONAL APPROACHES

A. Density-functional theory calculations

All calculations are performed using density-functional theory (DFT) as implemented in the Vienna *ab initio* simulation package (VASP) code [33,34]. The Kohn-Sham orbitals are expanded in a plane-wave basis set with a kinetic energy cutoff of up to 500 eV and the electron-ion interactions are described using the projector augmented wave (PAW) method [35,36]. We employ the semilocal generalized gradient approximation (GGA) due to Perdew, Burke, and Ernzerhof (i.e., Refs. [37] and [38]) for the exchange-correlation (xc) functional. To correct for the vdW effect, we follow the scheme of Grimme with two forms of damping functions—with zero damping (D3) and damping due to Becke and Johnson (D3BJ), following the set of parameters listed in Refs. [7,8,39]. These follow the internal parameter set (e.g., C_6 and R_{vdW}) as implemented in the VASP code. Here, we note that, similar to Ref. [40], we have also found anomalous values for the elastic constants using the earlier D2 scheme due to Grimme and have excluded them in this work. In addition, we have included DFT-PBE calculations based on the recent Tkatchenko-Scheffler (TS) vdW correction scheme [9], including the self-consistent long-range screening (SCS) term [10]. Lastly, we have also performed calculations based on four self-consistent nonlocal vdW-corrected functionals [15–18]—namely, vdW-DF1, vdW-DF2, optB86b, and optB88.

To afford a consistent **k**-point description for all calculations, we use a fairly dense **k**-point grid as generated by the γ-centered **k**-spacing method of $0.125\,\mathrm{\AA}^{-1}$ for all Brillouin-zone integrations. This setting corresponds to, for example, a $24 \times 24 \times 24$ **k**-point grid with 56 special **k** points in the irreducible Brillouin zone (IBZ) of the Cu primitive unit cell. The smearing method based on the Methfessel-Paxton scheme is used with a broadening of 0.1 eV to ease Brillouin-zone integrations. Using this dense number of **k** points, we perform structural optimization to obtain the equilibrium lattice constants and total energies, as well as various elastic constants, which will be discussed in the text below. All DFT calculations have been tested systematically for convergence whereby the total energy and forces on atoms are within 10^{-4} eV and $10^{-3}\,\mathrm{eV\AA}^{-1}$, respectively.

The equilibrium lattice constant, a_0, and the ground-state bulk modulus, B_0, are obtained by fitting the calculated total energies to the third-order Birch-Murnaghan equation of state [41,42]. To obtain the cohesive energy of system, E_{coh}, spin-polarized DFT calculations are performed for the metal atoms using a $15 \times 15.5 \times 16\,\mathrm{\AA}^3$ asymmetric cell. The asymmetry of this cell breaks the symmetry of the system, and thus helps to ensure the accurate ground-state electronic configuration of metals atoms is achieved where partial occupancies are prohibited [43].

The second-order elastic constants, C_{ij}, are defined by the curvature of the total energy plot with respect to the anisotropic strains applied about the equilibrium bulk positions of the atoms. In this work, we apply elastic deformations in step sizes of ± 0.001 and ± 0.002, ensuring the calculations of the second-order elastic constants converge to 1% (approximately less than 1 GPa). Here, for the calculation of the elastic constants, we have used the tetrahedron method with Blöchl corrections to ensure highly accurate total energies are obtained [44]. In all cases, the calculated elastic constants satisfy the Born's criteria for mechanical stability in a cubic crystal lattice [45].

Given that the calculation of these second-order C_{ij} are more sensitive to small errors made in the DFT total energies, we have carefully tested the convergence of their values for, e.g., applied deformation strain, number of **k** points used, and the kinetic energy cutoff for the expansion of the plane waves used in this work. Overall, we have found that the calculated C_{ij} values are less sensitive to the numerical error made in **k**-point sampling and the kinetic energy cutoff used, and this agrees with literature [46]. More important, we found that for total energy calculation at each deformation strain applied, the use of the tetrahedron method (with Blöch correction terms) [35,47] for the integration of the Brillouin zone is crucial to ensure that the energy-strain curves are smooth (i.e., without

unphysical kinks that may result in negative elastic constants). As a caution, we do notice that our C_{12} is generally slightly underestimated in certain isolated cases. For instance, using the PBE xc functional, we have calculated the C_{12} value of Cu to be 93 GPa, while the reported literature value averages at 121 GPa [44]. This 23% error bar is not small [45], but we find that this does not affect the results discussed in this work.

B. Elastic constants, elastic modulus, and anisotropic indices

These second-order elastic constants, also commonly known as the elastic stiffness tensor components C_{ij}, are useful for the determination of the compliance components, S_{ji}. From generalized Hooke's law, the defined linear functions for the stresses and strains are written as [48]

$$\sigma_i = C_{ij}\varepsilon_j, \tag{1}$$

$$\varepsilon_j = S_{ji}\sigma_i, \tag{2}$$

where $i,j = 1,2,\ldots,6$. The calculated stiffness C_{ij} is then used to resolve the corresponding S_{ji} by observing the relations given in Ref. [48], where

$$S_{11} = \frac{C_{11}+C_{12}}{C_{11}^2+C_{11}C_{12}-2C_{12}^2}, \tag{3}$$

$$S_{12} = -\frac{C_{12}}{C_{11}^2+C_{11}C_{12}-2C_{12}^2}, \tag{4}$$

$$S_{44} = \frac{1}{C_{44}}. \tag{5}$$

To complement the numerical method outlined above, we also consider an analytical approach to calculate the anisotropic Young's modulus E_{hkl} for a given $[hkl]$ direction. For cubic crystals, one can derive the following equation [48–51]:

$$\frac{1}{E_{hkl}} = S_{11} - 2S_A\frac{h^2k^2+k^2l^2+l^2h^2}{h^2+k^2+l^2}, \tag{6}$$

where $S_A = S_{11} - S_{12} - S_{44}/2$ are defined in Eqs. (3), (4), and (5).

In a similar fashion, one could also define the direction-dependent Poisson's ratio ν_{hkl} by calculating the applied stress along the $[hkl]$ direction (which is parallel to the $[hkl]$ vector, **n**) with the induced stress along the transverse direction **m** (which is normal to **n**), by averaging all components of **m** in the transverse direction [52].

To visualize these results in three-dimensional (3D) representation surfaces, we convert the coordination of $[hkl]$ into a spherical coordinates (r, φ, θ) system with a constant radius $(r = 1)$ for both the anisotropic Young's modulus as well as the anisotropic Poisson's ratio, where θ is the angle between the z Cartesian axis and **n** $(0 < \theta < \pi)$, and φ is the angle between the x Cartesian axis and the projection of **n** on the xy plane $(0 < \varphi < 2\pi)$ [52]. To give an example, the anisotropic Poisson's ratio is defined as a function of angles $\nu(\varphi,\theta)$, with the following equation:

$$\nu(\varphi,\theta) = -\frac{AS_{12}+B(S_{44}-2)}{16CS_{11}+16D(2S_{12}+S_{44})}, \tag{7}$$

where

$$A = 106 + 8\cos 2\theta + 14\cos 4\theta + 16\cos 4\varphi \sin^4\theta, \tag{8}$$

$$B = -11 + 4\cos 2\theta + 7\cos 4\theta + 8\cos 4\varphi \sin^4\theta, \tag{9}$$

$$C = 8\cos^4\theta + 6\sin^4\theta + 2\cos 4\varphi \sin^4\theta, \tag{10}$$

$$D = 2\sin^2 2\theta + 2\sin^4\theta \sin^2 2\varphi. \tag{11}$$

Similarly, a set of $E(\varphi,\theta)$ could be derived as well. Hereafter, the Cartesian $[hkl]$ system will be used interchangeably with the spherical (r, φ, θ) system in our discussion.

Lastly, we consider the commonly used anisotropic indices to measure the degree of anisotropy in these bulk coinage metals. These indices are useful to quantitatively discriminate the effect of the vdW corrections applied for each metal in this study, as well as among the metals themselves. Here, we introduce the Zener (A), Chung-Buessem (A^{C}), and universal (A^{U}) anisotropic indices, and for the cubic metals, they are defined as [53]

$$A = \frac{2C_{44}}{C_{11}-C_{12}}, \tag{12}$$

$$A^{\mathrm{C}} = \frac{3(A-1)^2}{3(A-1)^2+25A}, \tag{13}$$

$$A^{\mathrm{U}} = \frac{6}{5}\left(\sqrt{A}-\frac{1}{\sqrt{A}}\right). \tag{14}$$

By definition, if $A^{\mathrm{U}} = A^{\mathrm{C}} = 0$ and $A = 1$, the cubic crystal is ideally isotropic [53].

III. RESULTS AND DISCUSSION

A. Bulk equilibrium lattice properties and second-order elastic constants

There have already been a few systematic and detailed studies of the influence of the xc functional on the bulk lattice constants, cohesive energies, and isotropic bulk moduli of various metals and compounds (including the coinage metals Cu, Ag, and Au, which are studied in this work) [16,54,55]. It is not our aim to solely revisit and reproduce the results, but we have summarized our findings in the Supporting Information ([56], Fig. S1 and Table S1). There, we plot the bar-chart graphs of (a) the lattice constant, a_0, (b) the cohesive energy, E_{coh}, and (c) the isotropic bulk modulus, B_0 as a function of the various xc functionals listed in Sec. II. These bulk values are determined by fitting our DFT calculated values to a third-order Birch-Murnaghan equation of state. Overall, we find that our results agree with previous reported values with a mean absolute relative error (MARE) of 0.1% for a_0, 1.2% for E_{coh}, and 1.67% for B_0 [16,54].

Upon ensuring that our bulk lattice parameters agree well with other reported literatures, we now turn our attention to the higher order total energy derivative terms, namely the second-order elastic constants, C_{ij} [57]. Given the coinage metals (Cu, Ag, and Au) naturally crystallize in the cubic fcc lattice, we could reduce the elastic tensor to three terms, namely the C_{11}, C_{12}, and C_{44} constants. The calculated values are tabulated in Table S2 of the Supporting Information [56],

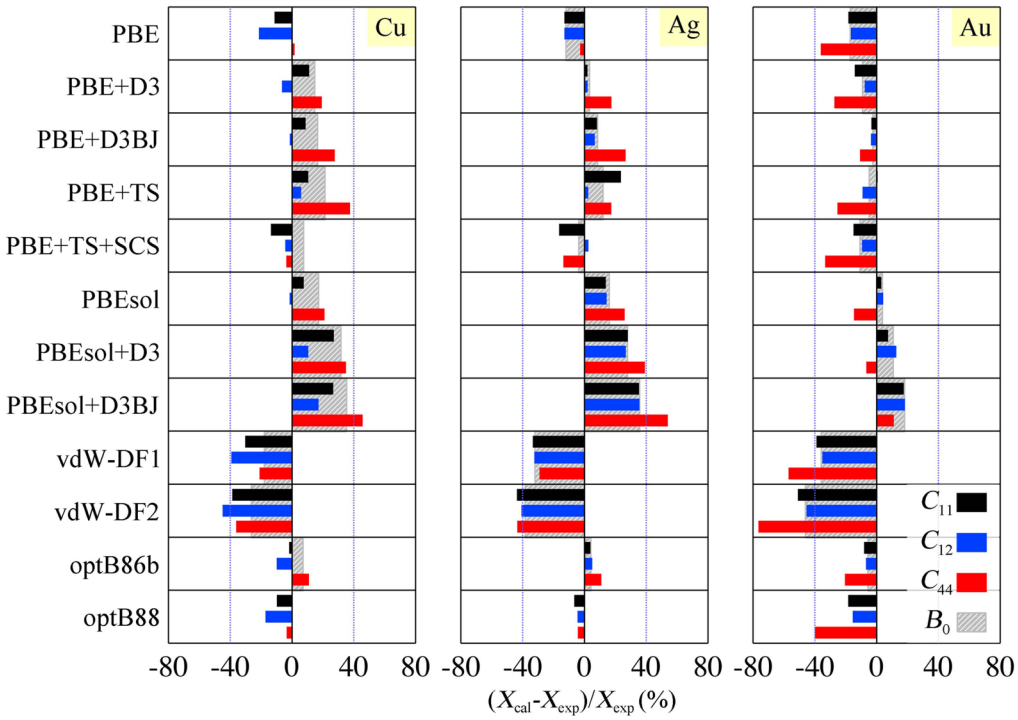

FIG. 1. The percentage relative error analysis for C_{ij} and B_0 in various vdW-corrected xc functionals. Here, X denotes either C_{ij} or B_0. The black, blue, and red bars are the relative errors (with respect to experimental values) of the calculated elastic constants, C_{11}, C_{12}, and C_{44}, respectively. The gray patterned bars are then the relative errors (with respect to experimental values) of the calculated bulk modulus, B_0, for each xc functional for Cu, Ag, and Au.

as well as shown graphically in Fig. S4. Here, we define the percentage relative errors via $(X_{cal} - X_{exp})/X_{exp} \times 100\%$, where X denotes the corresponding theoretically calculated (X_{cal}) and experimentally determined (X_{exp}) values for C_{11}, C_{12}, C_{44}, and B_0.

The experimental reference values used are averaged to minimize the dispersion of values found. These averaged elastic constants, $\bar{C}_{11}^{exp}$, $\bar{C}_{12}^{exp}$, and $\bar{C}_{44}^{exp}$, are 171.14, 122.62, and 73.92 GPa for Cu; 123.1, 92.6, and 46.1 GPa for Ag; and 188.0,159.0, and 42.15 GPa for Au, respectively [44,58–60]. From this set of averaged experimental elastic constants, in a similar fashion, we then determine an estimate of the (experimental) bulk modulus within the Voit-Ruess-Hill approximation, i.e., $\bar{B}_0^{exp} = (\bar{C}_{11}^{exp} + 2\bar{C}_{12}^{exp})/3$ [61,62]. These values are then used to compare with our calculated B_0 as obtained from using the third-order Birch-Murnaghan equation of state.

In Fig. 1, at a glance, the trend in the error bars for the C_{ij} values of all three coinage metals follow that of their B_0. In general, we notice that PBEsol tends to overestimate the elastic constants when compared to PBE, which agrees well with previous reports [16,54]. We find that including the non-self-consistent vdW corrected xc functionals of D3, D3BJ, and TS tends to overestimate the elastic constants when compared to the respective cases of PBE and PBEsol while TS+SCS narrows this gap.

To better understand the effect of these commonly used dispersion energy correction schemes to both PBE and PBEsol on the elastic constants, we plot the changes to the absolute values of the PBE and PBEsol calculated C_{ij} and B_0 for all three coinage metals upon applying these vdW corrections in Fig. 2. We define this change via the term ΔX where $\Delta X = X^{xc+vdW} - X^{xc}$ in which xc is the GGA in question (i.e., either PBE or PBEsol) and vdW refers to the applied vdW correction, namely, the D3, D3BJ, TS, and TS+SCS schemes.

From Fig. 2, we find that the force-field-type vdW corrections (Grimme's D3 and D3BJ) almost always increase the C_{ij} and B_0 values (i.e., $\Delta X > 0$) with a similar amount for both PBE and PBEsol (i.e., less sensitive to the starting GGA functional). Interestingly, we generally observe that the application of these vdW corrections do not increase the C_{ij} values by the same amount as $\Delta C_{11} > \Delta C_{12} > \Delta C_{44}$, with the exception of the D3 effect on Au. In particular, when comparing to the self-consistent PBE+TS and PBE+TS+SCS, we find that the latter greatly reduces the changes only in the C_{11} and C_{44} values in contrast to the former.

Returning to Fig. 1, we find a surprising opposite trend for the self-consistent vdW functionals, namely vdW-DF1, vdW-DF2, optB86b, and optB88. vdW-DF1 and vdW-DF2 greatly underestimate the elastic constants (up to 78% for Au), while the more recently refined optB86b and optB88 show much better agreement with available experimental data (with an exception to the C_{44} of Au). It has been previously reported that the vdW-DF1 and vdW-DF2 functionals are known to generally underestimate binding energies, which may have a direct consequence on its poor description of elastic properties [16].

Given that these self-consistent vdW functionals are constructed upon a semilocal GGA functional, it will be instructive to inspect the influence of the underlying GGA

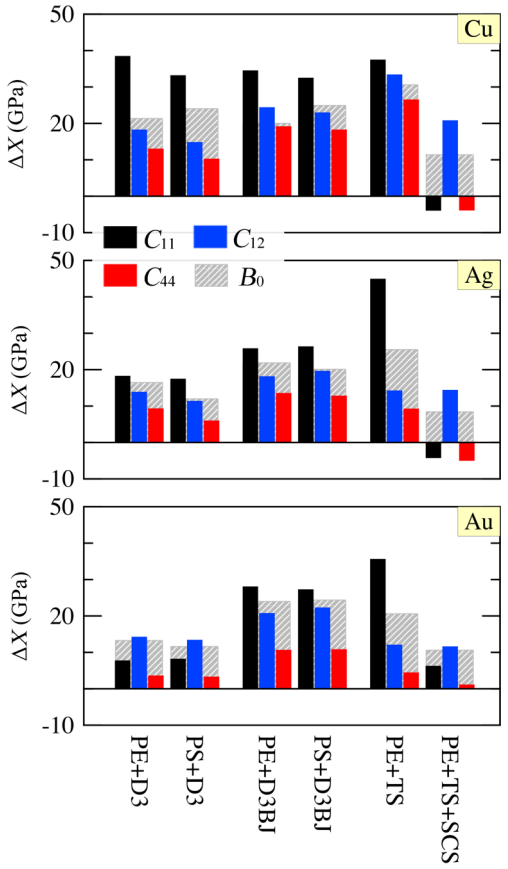

FIG. 2. Changes to the C_{ij} and B_0 of the coinage metals under the influence of various vdW corrections to the PBE and PBEsol xc functionals, namely, D3, D3BJ, TS, and TS+SCS. Here, X denotes either C_{ij} or B_0. The black, blue, and red bars are the relative errors (with respect to the corresponding PBE and PBEsol values) of the calculated elastic constants, C_{11}, C_{12}, and C_{44}, respectively. The gray patterned bars are then the relative errors (with respect to respective PBE and PBEsol values) of the calculated bulk modulus, B_0, for each xc functional for Cu, Ag, and Au.

functionals. Namely, the corresponding underlying GGAs for vdW-DF1, vdW-DF2, and optB86b are revPBE [63], rPW96 [64,65], and an optimized version of B86b, i.e., (opt)B86b [16], respectively. Using these underlying GGAs, we have performed additional calculations of the elastic constants at the equilibrium lattice constants determined using the corresponding vdW-corrected functionals. In Table I, we define $\Delta C_{ij}^{\rm vdw} = C_{ij}^{\rm vdW-xc} - C_{ij}^{\rm exp}$ and $\Delta C_{ij}^{\rm gga} = C_{ij}^{\rm unGGA} - C_{ij}^{\rm exp}$ where the calculated values using the vdW-corrected functionals ($C_{ij}^{\rm vdW-xc}$) and that with the underlying GGA ($C_{ij}^{\rm unGGA}$) are compared to those of experiments ($C_{ij}^{\rm exp}$).

We find that, indeed, the underlying GGA plays a non-negligible role, and as reported in Refs. [66] and [16], the gradient of the enhancement factor (F_x) with respect to a small reduced density gradient (s, around the $0 < s < 1$) in these GGAs is known to be important for describing the bulk properties of transition metals. In comparison, we find that the F_x varies as follows: rPW96 > revPBE ∼ PBE > optB88 > optB86b ∼ PBEsol [16,66], where rPW96 and revPBE show the steepest F_x for this low s range. As seen in Table I, it is already clear that (opt)B86b GGA yields a relatively small error ($\Delta C_{ij}^{\rm gga}$) as compared to that of revPBE and rPW96, and the errors in the calculated C_{ij} values ($\Delta C_{ij}^{\rm vdw}$) are carried over from the underlying GGA functionals (i.e., the relative ordering of $\Delta C_{44} < \Delta C_{11} < \Delta C_{12}$ is preserved), although reduced somewhat when corrected for vdW interactions.

From this analysis, we gather that optB86b (and similarly, optB88) not only increases the accuracy of describing the lattice constants, cohesive energies, and bulk moduli of these coinage metals but also provides a noticeable improvement in determining the elastic constants when compared to the semilocal PBE and PBEsol xc functionals.

B. Angular-dependent anisotropic mechanical properties

Collectively, these findings would then lead to the question if these modern-day vdW-corrected xc functionals are indeed accurate enough to describe angular-dependent anisotropic mechanical properties like the Young's modulus and the Poisson's ratio, which are a function of these second-order elastic constants. Indeed, it has very recently been reported that these vdW-corrected xc functionals can have a substantial effect on the stress-strain behavior of bulk metals like Pd [40].

After an overview of the effects of vdW corrections to the various bulk parameters and elastic constants along certain

TABLE I. Differences in the calculated elastic constants for Cu, Ag, and Au using various xc functionals keeping its equilibrium lattice constant as determined by the corresponding vdW-corrected functionals. We define $\Delta C_{ij}^{\rm vdw} = C_{ij}^{\rm vdW\text{-}xc} - C_{ij}^{\rm exp}$ and $\Delta C_{ij}^{\rm gga} = C_{ij}^{\rm unGGA} - C_{ij}^{\rm exp}$ where the calculated C_{ij} values of the vdW-corrected functionals (vdW-xc) and that of the underlying GGA (unGGA) are compared to those of experiments (exp). All values are reported in GPa.

Metal	vdW-xc/unGGA	$\Delta C_{11}^{\rm vdw}$	$\Delta C_{12}^{\rm vdw}$	$\Delta C_{44}^{\rm vdw}$	$\Delta C_{11}^{\rm gga}$	$\Delta C_{12}^{\rm gga}$	$\Delta C_{44}^{\rm gga}$
Cu	vdW-DF1/revPBE	− 51.9	− 48.1	− 15.5	− 56.0	− 55.2	− 12.6
	vdW-DF2/rPW96	− 66.2	− 55.1	− 26.7	− 71.8	− 63.9	− 24.0
	optB86b/(opt)B86b	− 3.3	− 12.2	8.1	− 8.1	− 19.3	11.2
Ag	vdW-DF1/revPBE	− 41.1	− 30.0	− 13.4	− 45.7	− 35.5	− 10.7
	vdW-DF2/rPW96	− 53.8	− 37.8	− 20.1	− 56.3	− 41.5	− 16.1
	optB86b/(opt)B86b	4.8	4.7	5.1	− 1.4	− 2.5	6.8
Au	vdW-DF1/revPBE	− 73.3	− 55.9	− 24.0	− 81.1	− 63.9	− 25.1
	vdW-DF2/rPW96	− 95.7	− 72.3	− 32.2	− 102.4	− 79.4	− 32.9
	optB86b/(opt)B86b	− 15.3	− 11.0	− 8.7	− 22.7	− 17.9	− 11.3

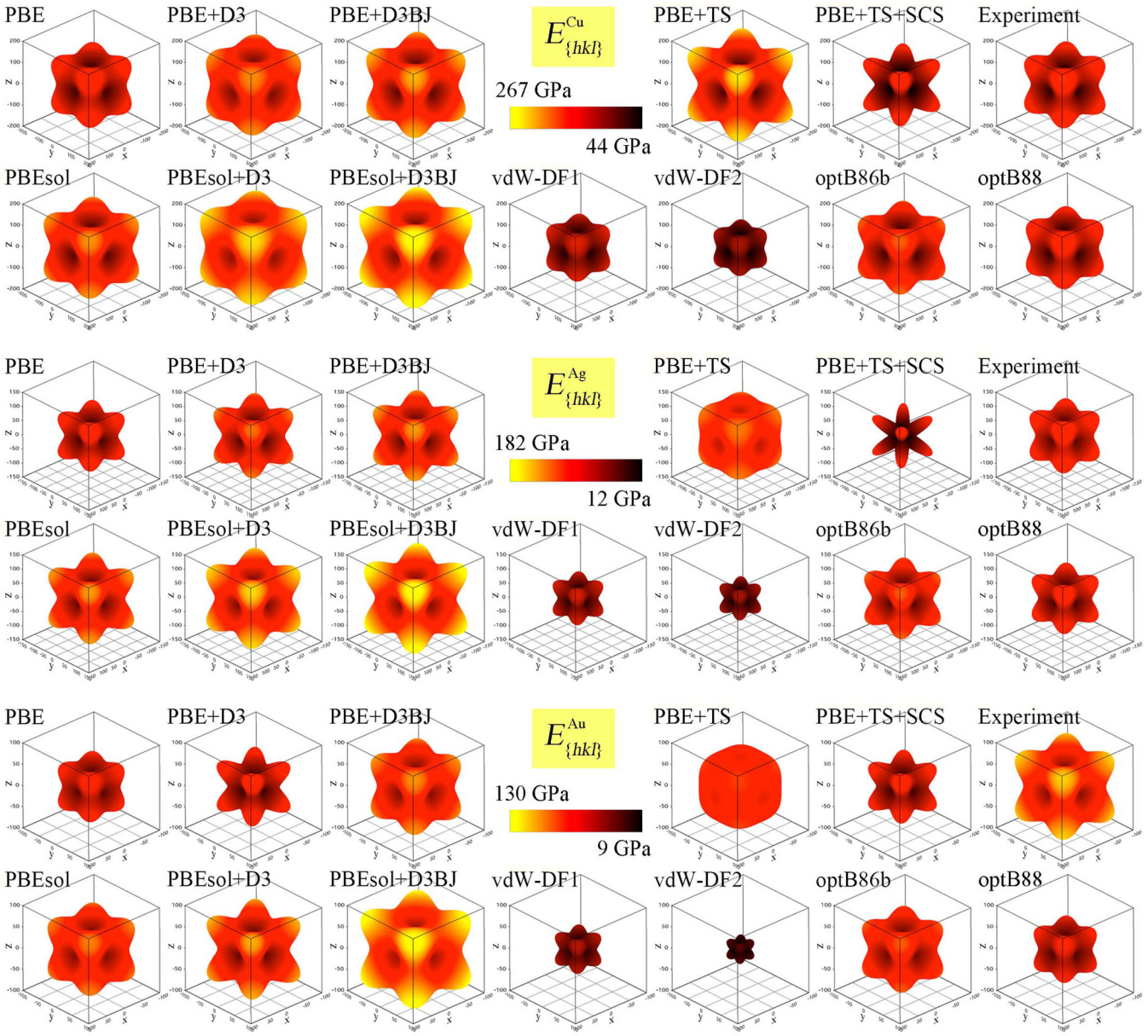

FIG. 3. Three-dimensional representation surfaces of the anisotropic Youngs modulus, E_{hkl}, of the coinage metals Cu, Ag, and Au. For each direction, the length of vectors is equated to the value of E_{hkl} (in units of GPa) where the range of values lie within the maxima (yellow) and minima (black) as indicated for each coinage metal.

high-symmetry directions (e.g., C_{11}, C_{12}, and C_{44}), we further extend our analysis to include multidirection dependencies, i.e., tracing the elastic mechanical responses of the coinage metals on a 3D representation surface under the influence of various vdW corrections to the xc functional.

To assess the accuracy of these various vdW-corrected xc functionals, we start by examining the anisotropic, angular-dependent (i.e., direction-dependent) Young's modulus, E_{hkl}, the fully reversible stiffness modulus as expressed within the linear elastic Hooke's law.

In Fig. 3, the angular dependence of E_{hkl} is graphically plotted for Cu, Ag, and Au within the PBE, PBEsol, and various vdW-corrected xc functionals. The three-dimensional (3D) polar plots based on experimental values for all three coinage metals are also shown for comparison, showing generally eight rounded protuberances at the corners in the {111} direction (cf., $3/(3S_{11} - 2S_A)$) and six depressed basins in the {100} direction (cf. $1/S_{11}$). The range of the plotting grids for the 3D surface plots of E_{hkl} is set to ± 200, ± 150, and ± 100 GPa for Cu, Ag, and Au, respectively, to portray the topology of the surfaces. Values of the S_{ij} are reported in Table S3 of the Supporting Information [56].

At a glance, for all xc functionals, the maxima and minima for all three coinage metals are found in the {111} and {100} directions, agreeing with previous literature [51]. This is very characteristic for fcc d metals, as opposed to highly isotropic metals like bcc W and fcc Al [49].

Referring to Fig. 3, we find that PBE, PBEsol, and their D3- and D3BJ-corrected counterparts capture the anisotropic 3D representation surfaces. The D3 and D3BJ vdW corrections

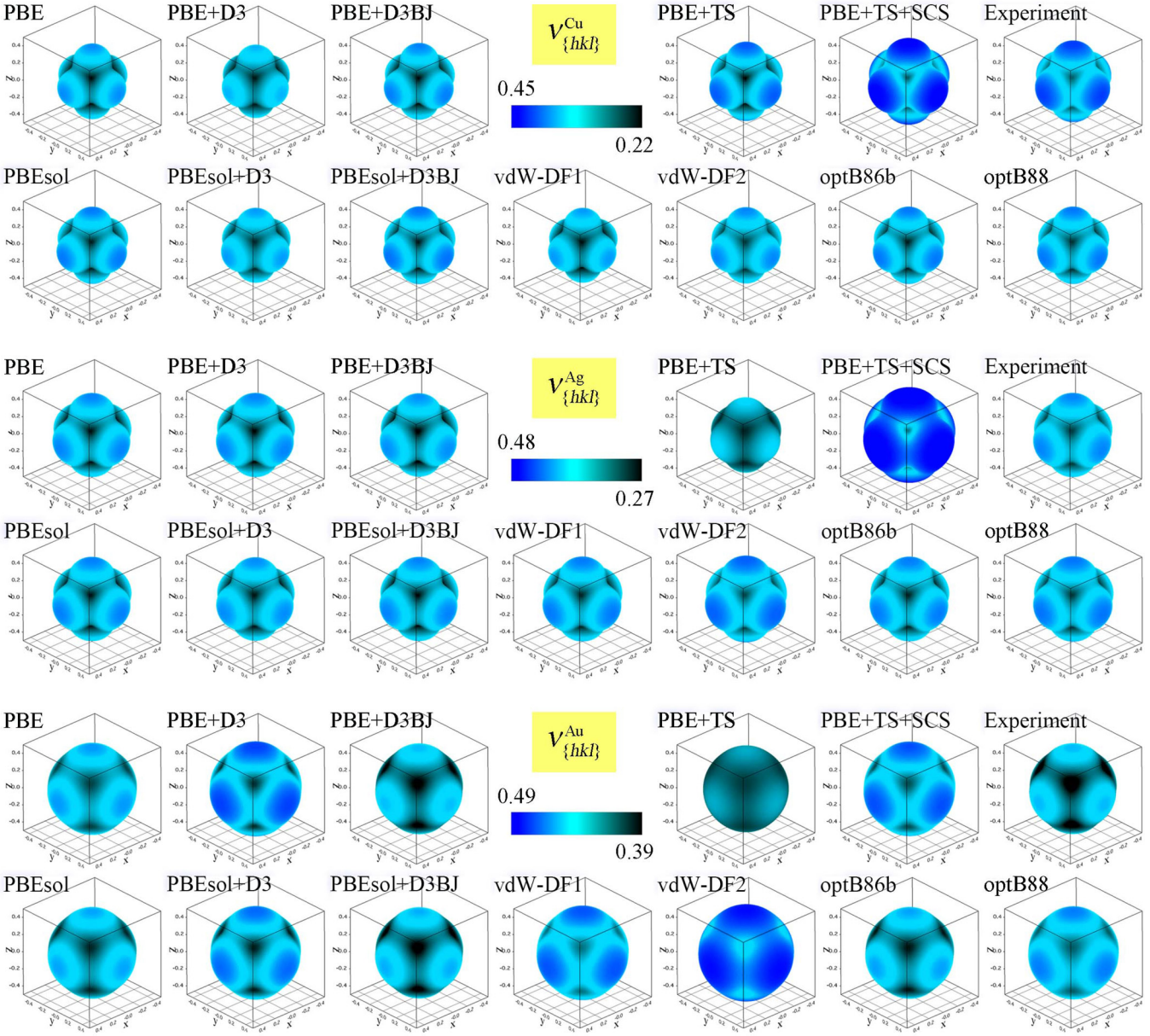

FIG. 4. Three-dimensional representation surfaces of the anisotropic Poisson's ratio, ν_{hkl}, of the coinage metals Cu, Ag, and Au. For each direction, the length of vectors is equated to the value of ν_{hkl} where the range of values lie within the maxima (blue) and minima (cyan) as indicated for each coinage metal.

generally increase the E_{hkl} values at the corners more than PBE and PBEsol, with D3BJ corrected xc functional having a larger increase. It is suggested that the BJ-damping function in the D3BJ correction includes more long-range interactions than the zero-damping function in D3 [2,8,10], and thus the D3BJ correction may further enhance the anisotropy in E_{hkl}.

We find that the PBE+TS xc functional greatly reduces the anisotropy in the E_{hkl} topology for Ag and Au, while slightly overestimating the E_{hkl} values for Cu when compared to the experimental E_{hkl} 3D topologies. For Ag and Au, PBE+TS yields an almost cubelike E_{hkl} topology, greatly reducing the E_{111}/E_{100} anisotropic ratio. More interestingly, after including self-consistent screening effects, the PBE+TS+SCS generally reduces the absolute values of E_{hkl} but sharply overestimates the E_{111}/E_{100} anisotropic ratio for all metals.

We attribute this acute increase in the E_{111}/E_{100} anisotropic ratio to the corresponding decrease in the metallic bonding along the {100} and {110} directions (see Table S4 of the Supporting Information [56]). Referring to the PBE+TS+SCS E_{hkl} 3D topology of Ag, it closely resembles the representation surface of an auxetic memory shape alloy, CuAlNi, as described in Ref. [67]. There, the memory shape alloy was also found to exhibit a negative Poisson's ratio in the [110] direction. This anisotropic weakening of the bond strength (along certain crystallographic directions) may be associated with the incorporated polarizability anisotropy in the construction of this TS+SCS correction to the PBE xc functional [2,10].

Evidently, the anisotropic 3D representation surfaces are best described by the self-consistent optB88 and optB86b vdW

xc functionals, giving a better balance between the overall 3D representation topology as well as the E_{111}/E_{100} anisotropy. This is especially true for Cu and Ag, while underestimating for more polarizable Au. On this note, it is necessary to mention that the vdW-DF1 and vdW-DF2 severely underestimate the E_{hkl} values, yielding rather unrealistic 3D topology profiles for all metals. This is closely linked to the underestimated C_{ij} values obtained with the vdW-DF1 and vdW-DF2 vdW xc functionals (see Fig. 1).

Now, we proceed to examine another anisotropic, angular-dependent (i.e., direction-dependent) mechanical property—the Poisson's ratio, ν_{hkl}, which is defined as the negative value of the ratio of the lateral (transverse) strain to the longitudinal strain. Using Eq. (7), we average the lateral responses for each longitudinal strain [52] and plot the normalized ν_{hkl} 3D representation surfaces for the three coinage metals within the PBE, PBEsol, and various vdW-corrected xc functionals in Fig. 4. (Tabulated values of ν_{hkl} can be found in Table S5 of the Supporting Information [56].) The range of the plotting grids in this case is set to ± 0.5 for Cu, Ag, and Au, respectively. We note that the negative scale of the 3D plot only reflects the direction, rather than an auxetic behavior.

The 3D surfaces based on the experimental ν_{hkl} values for Cu, Ag, and Au are also shown for comparison. The generic ν_{hkl} 3D profile for the coinage metals comprises six rounded protuberances along the {100} direction and eight depressed basins along the {111} direction. Considering the relative values of ν_{hkl} for these metals, we find that $\nu_{\mathrm{Cu}} < \nu_{\mathrm{Ag}} < \nu_{\mathrm{Au}}$, and this trend corroborates well with the experimental polycrystalline Poisson's ratios of 0.35, 0.37, and 0.42 for Cu, Ag, and Au, respectively [68].

Although the influence of the vdW corrections on the ν_{hkl} 3D representation surfaces is evident in Fig. 4, the extent is less pronounced than that of E_{hkl} 3D plots (as shown in Fig. 3). However, certain observations can be noted. The D3 and D3BJ corrections do not greatly change the original GGA 3D profiles for Cu and Ag, while for Au these Grimme-type vdW corrections show higher values of ν_{hkl} in D3 and smaller values of that in D3BJ, when compared to PBE and PBEsol. The PBE+TS tends to underestimate ν_{hkl} values while PBE+TS+SCS severely overestimates. Consistent with our observations for E_{hkl}, the ν_{hkl} 3D representation surfaces predicted with self-consistent optB88 and optB86b vdW xc functionals agree much better with the experimental plots (with optB86b providing the best agreement). Both the vdW-DF1 and vdW-DF2 vdW xc functionals predict a fairly similar 3D topology to experiments for Cu and Ag, but markedly overestimate for Au.

C. Elastic anisotropic indices

In retrospect, the influence of the vdW corrections to the PBE and PBEsol xc functionals investigated so far for the bulk lattice constants, second-order elastics constants, as well as the angular-dependent Young's modulus and Poisson's ratio of the three coinage metals is apparent but its measurable impact on the extent of elastic anisotropy of these metals is still rather ambiguous. Here, we adopt the numeric schemes due to Zener, Chung, and Ranganathan *et al.* [53,69,70] to quantify the elastic anisotropy in these coinage metals via the anisotropic indices of Zerner (A), Chung-Buessem (A^{C}), and the universal anisotropic index (A^{U}) [53]. According to Eq. (14), we then plot A and A^{C} as a function of A^{U} and include the error analysis of the predicted A^{U} for the three coinage metals in Fig. 5 (see also Table S6 of the Supporting Information [56]). The experimental A and A^{U} are derived from their corresponding experimental C_{ij} values, and are shown as dashed horizontal lines. The experimentally derived A^{U} (A) values for Cu, Ag, and Au are 1.65 (3.05), 1.62 (3.02), and 1.50 (2.91), respectively.

On a technical note, the Zener anisotropic index (A) can only be applied specifically to cubic systems and lacks the flexibility to handle noncubic crystal systems. However, for the case of fcc coinage metals, both A and A^{U} give the same information about anisotropy, and thus in the following analysis, we will simply refer only to the A^{U} index.

From Fig. 5, referring to the universal anisotropic index A^{U} (given in black lines), a departure from the zero value will truly reflect its extent of anisotropy and here we find a couple of outliers (i.e., more than 50% in error); namely the xc functional PBE+D3 strongly overestimates A^{U} of Cu, PBE+TS strongly underestimates that of both Ag and Au, and PBE+TS+SCS severely overestimates A^{U} of all coinage metals (especially so for Ag and Cu). Statistically speaking, without considering these outliers PBE+TS and PBE+TS+SCS, we find that the calculated A^{U} values for Au varies with a standard deviation of 0.56 (or 0.71 with them included), while Ag and Cu have smaller standard deviations of 0.23 and 0.17, respectively. Across all xc functionals tested, optB86b provides the most balanced description of elastic anisotropies in these coinage metals with the smallest average error. Notably, PBEsol+D3BJ yields the smallest absolute error in A^{U} for both Cu and Au, but a 25% for Ag.

We attempt to understand these anomalies by inspecting the calculated 3D representation surfaces of E_{hkl} (as shown in Fig. 3). For instance, using the PBE+TS+SCS xc functional, we find that both the E_{100} and E_{110} values of Ag are so strongly underestimated (as compared to that of E_{111}) that it results in the grossly overestimated A^{U} value of 9.81. In comparison to other cubic metals, this poor (and wrong) description predicts Ag to be much more anisotropic than Pb or Cs, which would usually have a value of 2.6 for A^{U} [53]. In the other extreme case, using the xc functional PBE+TS to predict the A^{U} of Ag and Au fails badly, yielding near-isotropic values of 0.50 and 0.14, respectively. Once again, this is clearly shown by the almost cubic 3D representation surfaces of E_{hkl} for these metals in Fig. 3, where the E_{100} and E_{110} values are overestimated while that of E_{111} is underestimated. This failure of PBE+TS may wrongly suggest that Ag and Au are more similar to the isotropic W or Co [53].

D. Error analysis of anisotropic mechanical properties

Finally, in order to assess how much of the error in these anisotropic properties is inherited from the intrinsic errors in the equilibrium properties of the coinage metals (i.e., lattice constants), we have also recalculated the C_{ij} values with the various xc functionals at the experimental lattice constant for all three coinage metals to decompose the influence of the different lattice parameters and the C_{ij} values predicted by

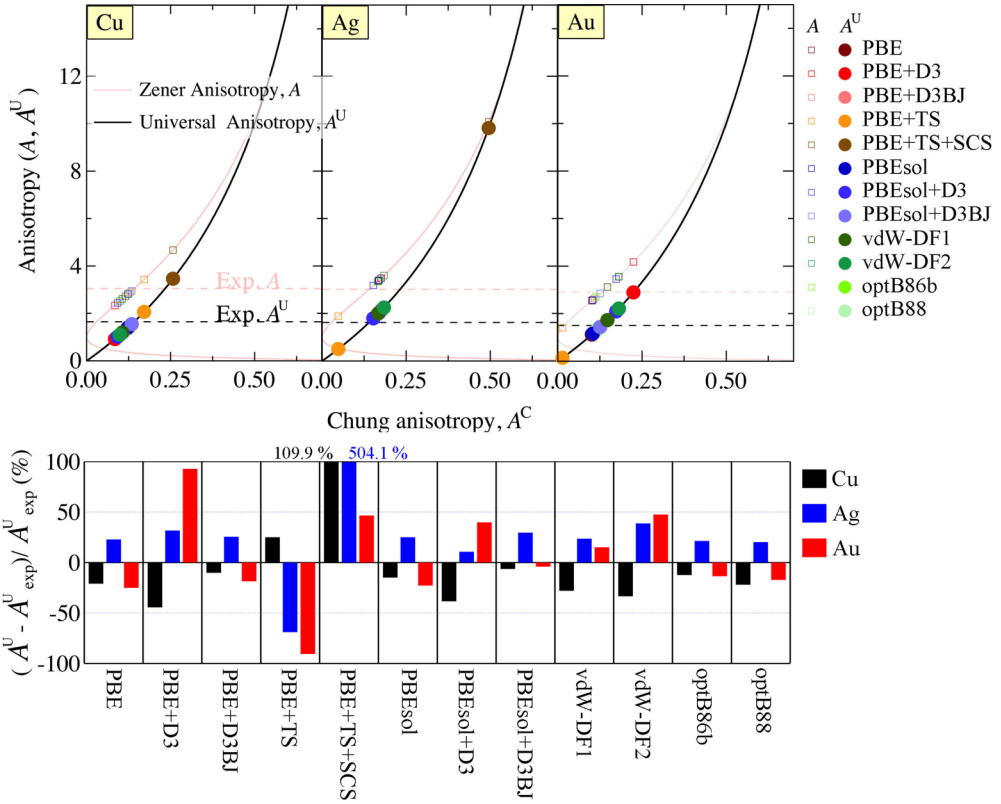

FIG. 5. Upper panel: Elastic anisotropic indices of Cu, Ag, and Au. The Zener anisotropy (A) and universal anisotropy (A^{U}) indices are plotted as a function of Chung's anisotropy index (A^{C}). For each coinage metal, the calculated values are color coded for each xc functional as shown in the legend on the right. Lower panel: The percentage relative error (in %) in the calculated A^{U} (with respect to the experimental A^{U}) are shown for Cu (in black bars), Ag (in blue bars), and Au (in red bars) for each xc functional. The experimentally derived A^{U} (A) values for Cu, Ag, and Au are 1.65 (3.05), 1.62 (3.02), and 1.50 (2.91), respectively.

different xc functionals. This result is illustrated together as a plot of calculated C_{ij} values as a function of the calculated lattice constants in Fig. 6 (see also Table S7 of Supporting Information [56]).

Here, we observe that the calculated C_{ij} values vary almost linearly with varying lattice constant values. Interestingly, from Fig. 2, we notice that the gradient of variation for the C_{44} of Au is the most gentle when compared to that for C_{11} and C_{12} of the same metal. On the other hand, the gradients of variation for the C_{ij} of Ag are most similar. Overall, confining our discussion to only using the experimental lattice constants, we do find an improved agreement with experimental C_{ij} values. Nonetheless, the ordering of the universal anisotropic index for these metals is not changed (see Table S7). We therefore argue that there is a non-negligible influence of vdW corrections to the anisotropic mechanical properties of these coinage metals with minimal influence from the equilibrium lattice constants.

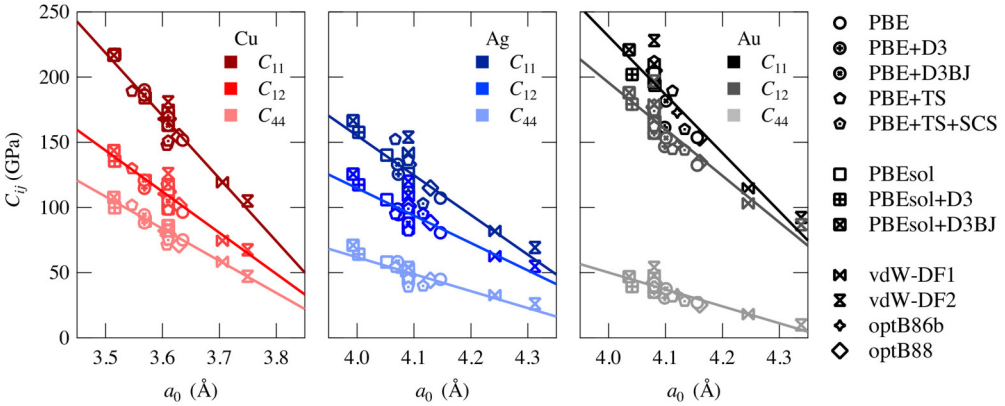

FIG. 6. Calculated C_{11}, C_{12}, and C_{44} values using the various xc functionals plotted as a function of the correspondingly determined lattice constant, a_0. Values of C_{ij} as calculated using the experimental lattice constants are also included for discussion.

IV. CONCLUSIONS

In summary, using a range of vdW-corrected xc DFT functionals, we have calculated and critically assessed the influence of the vdW contribution to the anisotropic mechanical properties of Cu, Ag, and Au. Besides agreeing well with previous theoretical reports on the lattice constant and cohesive energy values, we have found that applying the various types of vdW corrections to the second-order elastic constant (C_{ij}) calculations produced a mixed bag of results. The force-field type (D3 and D3BJ) and self-consistent TS corrections tend to overestimate the C_{ij} values when compared to the ones calculated by the noncorrected PBE and PBEsol while TS+SCS narrows this gap. On the other hand, the nonlocal vdW-DF1 and vdW-DF2 functionals grossly underestimate the C_{ij} values, while the optB86b and optB88 offered the best agreement with available experimental data.

Using these calculated C_{ij} values, we have proceeded to plot the angular-dependent anisotropic mechanical properties, namely the Young's modulus (E_{hkl}) and Poisson's ratio (ν_{hkl}) via 3D representation surfaces. It is found that the vdW correction scheme due to Grimme (D3 and D3BJ) agree only fairly with the experimental 3D topology, while the TS and TS+SCS methods fail to describe the correct anisotropic topology of both E_{hkl} and ν_{hkl}, especially for Ag and Au. Due to their severely underestimated C_{ij} values, the nonlocal vdW-DF1 and vdW-DF2 functionals have predicted rather unrealistic 3D topology profiles for all metals. Once again, the optB86b and optB88 xc functionals provide the closet angular-dependent anisotropic topology profiles to the experimental ones for E_{hkl} and ν_{hkl}. A quantitative analysis of the universal anisotropic index A^{U} corroborates with the consistent balanced performance of the nonlocal optB86b and optB88 xc functionals in describing the extent of elastic anisotropy in these coinage metals.

We believe that this examination of the influence of vdW corrections on the less-studied (albeit, important) anisotropic mechanical properties of coinage metals points to the fact that advocating a perfect vdW-inclusive xc functional for describing the general physics and chemistry of these coinage metal may be a little premature. In the context of this work, we believe that these challenges to modern DFT xc functionals for anisotropically strained coinage metals (e.g., at the faceted surfaces of nanostructures) may be very relevant to other strained material systems.

ACKNOWLEDGMENTS

The authors acknowledge the support of National Research Foundation (NRF) of Korea funded by the Ministry of Education, Science, and Technology (NRF Grant No. 2014R1A1A1003415) and the providing of computational resources by the Korean Institute of Science and Technology Information (KISTI) supercomputing center through the strategic support program for supercomputing application research (KSC-2015-C3-043). We thank J. W. Park for the helpful discussion regarding the use of vdW corrections in the VASP code and Y. G. Jung for helping in the data organization and discussion of this paper.

[1] K. Lejaeghere, G. Bihlmayer, T. Björkman, P. Blaha, S. Blügel, V. Blum, D. Caliste, I. E. Castelli, S. J. Clark, A. Dal Corso, S. de Gironcoli, T. Deutsch, J. K. Dewhurst, I. Di Marco, C. Draxl, M. Dułak, O. Eriksson, J. A. Flores-Livas, K. F. Garrity, L. Genovese, P. Giannozzi, M. Giantomassi, S. Goedecker, X. Gonze, O. Grånäs, E. K. U. Gross, A. Gulans, F. Gygi, D. R. Hamann, P. J. Hasnip, N. A. W. Holzwarth, D. Iuşan, D. B. Jochym, F. Jollet, D. Jones, G. Kresse, K. Koepernik, E. Küçükbenli, Y. O. Kvashnin, I. L. M. Locht, S. Lubeck, M. Marsman, N. Marzari, U. Nitzsche, L. Nordström, T. Ozaki, L. Paulatto, C. J. Pickard, W. Poelmans, M. I. J. Probert, K. Refson, M. Richter, G.-M. Rignanese, S. Saha, M. Scheffler, M. Schlipf, K. Schwarz, S. Sharma, F. Tavazza, P. Thunström, A. Tkatchenko, M. Torrent, D. Vanderbilt, M. J. van Setten, V. Van Speybroeck, J. M. Wills, J. R. Yates, G.-X. Zhang, and S. Cottenier, Science **351**, aad3000 (2016).

[2] J. Klimeš and A. Michaelides, J. Chem. Phys. **137**, 120901 (2012).

[3] A. M. Reilly and A. Tkatchenko, Chem. Sci. **6**, 3289 (2015).

[4] S. Grimme, J. Comput. Chem. **27**, 1787 (2006).

[5] A. Tkatchenko, Adv. Funct. Mater. **25**, 2054 (2015).

[6] M. Kim, W. J. Kim, E. K. Lee, S. Lebgue, and H. Kim, Int. J. Quantum Chem. **116**, 598 (2016).

[7] S. Grimme, J. Antony, S. Ehrlich, and H. Krieg, J. Chem. Phys. **132**, 154104 (2010).

[8] S. Grimme, S. Ehrlich, and L. Goerigk, J. Comput. Chem. **32**, 1456 (2011).

[9] A. Tkatchenko and M. Scheffler, Phys. Rev. Lett. **102**, 073005 (2009).

[10] A. Tkatchenko, R. A. DiStasio, Jr., R. Car, and M. Scheffler, Phys. Rev. Lett. **108**, 236402 (2012).

[11] T. Bučko, S. Lebègue, J. Hafner, and J. G. Ángyán, Phys. Rev. B **87**, 064110 (2013).

[12] K. Rapcewicz and N. W. Ashcroft, Phys. Rev. B **44**, 4032 (1991).

[13] Y. Andersson, D. C. Langreth, and B. I. Lundqvist, Phys. Rev. Lett. **76**, 102 (1996).

[14] J. F. Dobson and B. P. Dinte, Phys. Rev. Lett. **76**, 1780 (1996).

[15] M. Dion, H. Rydberg, E. Schröder, D. C. Langreth, and B. I. Lundqvist, Phys. Rev. Lett. **92**, 246401 (2004).

[16] J. Klimeš, D. R. Bowler, and A. Michaelides, Phys. Rev. B **83**, 195131 (2011).

[17] J. Klimeš, D. R. Bowler, and A. Michaelides, J. Phys.: Condens. Matter **22**, 022201 (2010).

[18] K. Lee, E. D. Murray, L. Kong, B. I. Lundqvist, and D. C. Langreth, Phys. Rev. B **82**, 081101(R) (2010).

[19] C. Li, T. Winzer, A. Walsh, B. Yan, C. Stampfl, and A. Soon, Phys. Rev. B **90**, 075438 (2014).

[20] E. N. Voloshina, Y. S. Dedkov, S. Torbrügge, A. Thissen, and M. Fonin, Appl. Phys. Lett. **100**, 241606 (2012).

[21] J. Hwang, M. Kim, D. Campbell, H. A. Alsalman, J. Y. Kwak, S. Shivaraman, A. R. Woll, A. K. Singh, R. G. Hennig, S. Gorantla, M. H. Rümmeli, and M. G. Spencer, ACS Nano **7**, 385 (2013).
[22] L. Ferrighi, M. I. Trioni, and C. D. Valentin, J. Phys. Chem. C **119**, 6056 (2015).
[23] T. Björkman, A. Gulans, A. V. Krasheninnikov, and R. M. Nieminen, J. Phys.: Condens. Matter **24**, 424218 (2012).
[24] C. R. C. Rêgo, L. N. Oliveira, P. Tereshchuk, and J. L. F. D. Silva, J. Phys.: Condens. Matter **27**, 415502 (2015).
[25] T. Bučko, J. Hafner, S. Lebègue, and J. G. Ángyán, J. Phys. Chem. A **114**, 11814 (2010).
[26] W. Gao and A. Tkatchenko, Phys. Rev. Lett. **114**, 096101 (2015).
[27] G. Graziano, J. Klimeš, F. Fernandez-Alonso, and A. Michaelides, J. Phys.: Condens. Matter **24**, 424216 (2012).
[28] J. J. Rehr, E. Zaremba, and W. Kohn, Phys. Rev. B **12**, 2062 (1975).
[29] V. G. Ruiz, W. Liu, E. Zojer, M. Scheffler, and A. Tkatchenko, Phys. Rev. Lett. **108**, 146103 (2012).
[30] J. Carrasco, W. Liu, A. Michaelides, and A. Tkatchenko, J. Chem. Phys. **140**, 084704 (2014).
[31] W. Liu, F. Maaß, M. Willenbockel, C. Bronner, M. Schulze, S. Soubatch, F. S. Tautz, P. Tegeder, and A. Tkatchenko, Phys. Rev. Lett. **115**, 036104 (2015).
[32] V. G. Ruiz, W. Liu, and A. Tkatchenko, Phys. Rev. B **93**, 035118 (2016).
[33] G. Kresse and J. Furthmüller, Phys. Rev. B **54**, 11169 (1996).
[34] G. Kresse and J. Furthmüller, Comput. Mater. Sci. **6**, 15 (1996).
[35] P. E. Blöchl, Phys. Rev. B **50**, 17953 (1994).
[36] G. Kresse and D. Joubert, Phys. Rev. B **59**, 1758 (1999).
[37] J. P. Perdew, K. Burke, and M. Ernzerhof, Phys. Rev. Lett. **77**, 3865 (1996).
[38] J. P. Perdew, A. Ruzsinszky, G. I. Csonka, O. A. Vydrov, G. E. Scuseria, L. A. Constantin, X. Zhou, and K. Burke, Phys. Rev. Lett. **100**, 136406 (2008).
[39] L. Goerigk and S. Grimme, Phys. Chem. Chem. Phys. **13**, 6670 (2011).
[40] N. V. Ilawe, J. A. Zimmerman, and B. M. Wong, J. Chem. Theory Comput. **11**, 5426 (2015).
[41] F. Birch, Phys. Rev. **71**, 809 (1947).
[42] A. O. de-la Roza and V. Luaa, Comput. Phys. Commun. **182**, 1708 (2011).
[43] S.-H. Yoo, J.-H. Lee, Y.-K. Jung, and A. Soon, Phys. Rev. B **93**, 035434 (2016).
[44] Y. Le Page and P. Saxe, Phys. Rev. B **65**, 104104 (2002).
[45] F. Mouhat and F.-X. Coudert, Phys. Rev. B **90**, 224104 (2014).
[46] M. Łopuszyński and J. A. Majewski, Phys. Rev. B **76**, 045202 (2007).
[47] M. Methfessel and A. T. Paxton, Phys. Rev. B **40**, 3616 (1989).
[48] J. F. Nye, *Physical Properties of Crystals: Their Representation by Tensors and Matrices* (Oxford University Press, London, 1985).
[49] J.-M. Zhang, Y. Zhang, K.-W. Xu, and V. Ji, Physica B (Amsterdam, Neth.) **390**, 106 (2007).
[50] X. Li, S. Schönecker, J. Zhao, B. Johansson, and L. Vitos, Phys. Rev. B **87**, 214203 (2013).
[51] J.-M. Zhang, Y. Zhang, K.-W. Xu, and V. Ji, J. Phys. Chem. Solids **68**, 503 (2007).
[52] K. W. Wojciechowski, CMST **11**, 73 (2005).
[53] S. I. Ranganathan and M. Ostoja-Starzewski, Phys. Rev. Lett. **101**, 055504 (2008).
[54] J. Park, B. D. Yu, and S. Hong, Curr. Appl. Phys. **15**, 885 (2015).
[55] D. J. Carter and A. L. Rohl, J. Chem. Theory Comput. **8**, 281 (2012).
[56] See Supplemental Material at http://link.aps.org/supplemental/10.1103/PhysRevB.94.024108 for detailed description of the anisotropic mechanical calculations of these coinage metals.
[57] H. Wang and M. Li, Phys. Rev. B **79**, 224102 (2009).
[58] C. Kittel, *Introduction to Solid State Physics*, 6th ed. (John Wiley & Sons, New York, 1986).
[59] C. Teodosiu, *Elastic Models of Crystal Defects* (Springer-Verlag, New York, 1985).
[60] D. Pierce, K. Nowag, A. Montagne, J. Jimnez, J. Wittig, and R. Ghisleni, Mater. Sci. Eng., A **578**, 134 (2013).
[61] B. D. Fulcher, X. Y. Cui, B. Delley, and C. Stampfl, Phys. Rev. B **85**, 184106 (2012).
[62] E. Schreiber, O. Anderson, and N. Soga, *Elastic Constants and Their Measurements* (McGraw-Hill Education, New York, 1974).
[63] Y. Zhang and W. Yang, Phys. Rev. Lett. **80**, 890 (1998).
[64] O. A. Vydrov and T. Van Voorhis, J. Chem. Phys. **133**, 244103 (2010).
[65] J. P. Perdew and W. Yue, Phys. Rev. B **33**, 8800(R) (1986).
[66] G. I. Csonka, J. P. Perdew, A. Ruzsinszky, P. H. T. Philipsen, S. Lebègue, J. Paier, O. A. Vydrov, and J. G. Ángyán, Phys. Rev. B **79**, 155107 (2009).
[67] T. Paszkiewicz and S. Wolski, J. Phys.: Conf. Ser. **104**, 012038 (2008).
[68] S. Pugh, Philos. Mag. **45**, 823 (1954).
[69] D. H. Chung and W. R. Buessem, J. Appl. Phys. **38**, 2010 (1967).
[70] C. Zener, *Elasticity and Anelasticity of Metals* (University of Chicago, Chicago, 1948).